Journal of Alloys and Compounds 699 (2017) 308–322

Contents lists available at ScienceDirect

Journal of Alloys and Compounds

journal homepage: http://www.elsevier.com/locate/jalcom

Mechanical, thermal and electrical properties of monolayer and bilayer graded Al/SiC/rice husk ash (RHA) composite

A. Bahrami [a, b, *], N. Soltani [a, b], S. Soltani [c], M.I. Pech-Canul [a], L.A. Gonzalez [a], C.A. Gutierrez [a], A. Möller [d], J. Tapp [d], A. Gurlo [e]

[a] Centro de Investigación y de Estudios Avanzados del IPN Unidad Saltillo, Ave. Industria Metalúrgica No. 1062, Parque Industrial Saltillo-Ramos Arizpe, Ramos Arizpe, 25900 Coahuila, Mexico
[b] Instituto de Investigaciones en Materiales, Universidad Nacional Autónoma de México, Ciudad Universitaria, 04510 D.F., Mexico
[c] Faculty of Electrical and Computer Engineering, K. N. Toosi University of Technology, 16314 Tehran, Iran
[d] Institute of Inorganic and Analytical Chemistry, Johannes Gutenberg-University Mainz, Duesbergweg 10-14, 55128 Mainz, Germany
[e] Fachgebiet Keramische Werkstoffe/Chair of Advanced Ceramic Materials, Institut für Werkstoffwissenschaften und –technologien, Technische Universitaet Berlin, Hardenbergstraße 40, 10623 Berlin, Germany

ARTICLE INFO

Article history:
Received 25 November 2016
Accepted 26 December 2016
Available online 29 December 2016

Keywords:
Pressureless infiltration
Bending strength
Coefficient of thermal expansion
Electrical resistivity
Thermal diffusivity

ABSTRACT

The mechanical, electrical and thermal properties as well as thermal expansion of Al/SiC/RHA (rice husk ash) monolayer and bilayer composite have been studied using the Taguchi method and analysis of variance (ANOVA). The parameter that most significantly affects the modulus of elasticity of Al/SiC/RHA bilayer composites is processing time, with contribution percentages of 68 and 27% calculated from stress-strain graphs and ultrasonic method, respectively. However, the factor which mostly affects bending strength, CTE value and electrical resistivity of composites is process temperature with contribution percentages of 32, 28, and 22%, respectively. The projected values for modulus of elasticity (170 GPa), bending strength (369 MPa), CTE (8.9×10^{-6}/°C) and electrical resistivity (0.0019 Ω m) of Al/SiC/RHA composites are in excellent agreement with those obtained in the verification tests under the optimal conditions according to ANOVA.

1. Introduction

For some applications, composite materials are considered to be more suitable than conventional materials as they have desirable mechanical, thermal, electrical and wear properties. Among them, particulate reinforced composites (PMMCs) have attracted considerable attention due to their relatively low costs and inherent isotropic properties [1–3]. Metal matrix composites containing 25–60 vol % ceramic particulate in a high-strength matrix alloy have properties which are attractive for multifunctional electronic packaging, mirror substrates and support structures in optical systems, and components for inertial guidance systems [4–6]. The key requirements for this application are a high thermal conductivity and a coefficient of thermal expansion (CTE) similar to that of materials commonly used in microelectronic systems [7]. Among the different composites that are nowadays being considered for these applications, Al/SiC composites with a high-volume fraction of particulate reinforcement are a suitable and versatile option due to outstanding physical properties of SiC particles (High thermal conductivity, low CTE value and electrical conductivity). Although the Infiltration of ceramic preforms by liquid metals has been typically applied for the processing of composite materials with high percentage of reinforcement [8,9], as a constitutive route, it offers the potential for the production of graded composite materials by variation of shape, size, and volume fraction of the reinforcement in each layer. Successful fabrication of bilayer graded Al/SiC/RHA composite by pressureless infiltration method has been reported elsewhere [10]. In addition to the outstanding properties of RHA in different sectors such as cement industry, electronics, catalyst supports and etc. [11,12], recently it is widely used in fabrication of hybrid metal matrix composite materials [13]. Although SiO_2 derived from rice husk is by nature non-wettable, embedment of amorphous and crystalline SiO_2-derived RHA into SiC substrates up to 20 wt% will not make the system non-wettable

* Corresponding author. Centro de Investigación y de Estudios Avanzados del IPN Unidad Saltillo, Ave. Industria Metalúrgica No. 1062, Parque Industrial Saltillo-Ramos Arizpe, Ramos Arizpe, 25900 Coahuila, Mexico.
E-mail addresses: amin.bahrami@iim.unam.mx, amin.bah@gmail.com (A. Bahrami).

http://dx.doi.org/10.1016/j.jallcom.2016.12.339
0925-8388/

by Al-Si-Mg alloys [14]. RHA act as an oxygen donator to form MgO and $MgAl_2O_4$ in the Al/SiC/RHA system and as a results fabrication of hybrid composite. Also, in presence of amorphous RHA the formation of deleterious phase of Al_4C_3 was eliminated. Significant increase in hardness of fabricated hybrid Al/SiC/RHA composite in comparison to the conventional Al/SiC composite were observed [10].

In the present work, the quantitative effect of processing parameters on the bending strength and modulus of elasticity as well as physical properties such as electrical resistivity, CTE value and thermal diffusivity of monolayer and bilayer Al/SiC/RHA composite are investigated. The optimum conditions for abovementioned mechanical and physical properties of composites are projected and the infiltration characteristics under optimum conditions are determined and verified.

2. Experimental procedure

Infiltration tests for composites of Al/SiC/RHA were conducted under the conditions shown in Table 1. The effect of various parameters on the mechanical and physical properties of composite were investigated using the Taguchi method for design of experiments [15]. Infiltration temperature, time, particle size, porosity, SiO_2 crystallinity and content in the bilayer preform were used as parameters of infiltration process. The fabrication method as well as fabrication conditions have been discussed in details elsewhere [10]. Table 2 show L27 Taguchi tables used for this study.

Specimens for microstructure analysis were mounted and polished using standard metallurgical procedures, and the analysis was done using X-ray diffraction (XRD), scanning electron microscopy (SEM) and energy dispersive X-rays (EDXs). The elastic modulus and bending strength of all fabricated monolayer and bilayer composites were determined using bend test bars of dimensions 2 × 1.5 × 25 mm. The bending strength was measured in the four-point mode taking into account the compliance of the test system. The support distances were 10 mm and 20 mm. The elastic modulus was calculated from the first resonant frequency of the bar in accordance with ASTM C1161-13 [16].

Coefficient of thermal expansion (CTE), Electrical resistivity and thermal diffusivity of all fabricated composite were measured in this study. CTE values were measured by TMA 402 F1/F3 Hyperion®, a Thermomechanical Analyzer - Vertical Dilatometer. Samples were cut from the alloys and composite with the size of 3 × 3 × 2 mm. Both crystalline and amorphous silica were heated up to 1000 °C, while the temperature of 300 °C was chosen for aluminum alloys and composites. All samples were heated up and cooled down with the rate of 20 °C/min under protective atmosphere of high purity nitrogen with the flow rate of 30 cm^3/min.

Electrical resistivity and conductivity were measured using four-point probe technique (Lucas Labs S-302 Four Point Probe) on the flat faces of the samples. The measurement was conducted using direct current (DC) in order to avoid skin effects associated with AC current in the matrix and transient polarization phenomena in the ceramic component. To eliminate thermoelectric and capacity effects of the setup, the direction of the current was repeatedly reversed manually and the average of the absolute value of the two measured voltage drops was taken. The two values usually differed by less than 1% of their average. To avoid systematic errors, similar specimens were cut from the unreinforced matrix material and tested under the same conditions. The reliability of the measurements was assessed by measuring a sample 10 times

Table 2
Standard L27 Taguchi table designed for pressureless infiltration process of SiC/RHA preform.

No.	A	B	C	D	E	F	G	H	I	Explanation
1	1	1	1	1	1	1	1	1	1	CI
2	1	1	1	1	2	2	2	2	2	CI
3	1	1	1	1	3	3	1•	3	3	CI
4	1	2	2	2	1	1	1	2	2	PI
5	1	2	2	2	2	2	2	3	3	PI
6[a]	1	2	2	2	3	3	1•	1	1	CI
7	1	3	3	3	1	1	1	3	3	CI
8	1	3	3	3	2	2	2	1	1	CI
9	1	3	3	3	3	3	1•	2	2	CI
10	2	1	2	3	1	2	1•	1	2	PI
11	2	1	2	3	2	3	1	2	3	CI
12	2	1	2	3	3	1	2	3	1	NI
13	2	2	3	1	1	2	1•	2	3	CI
14[a]	2	2	3	1	2	3	1	3	1	CI
15	2	2	3	1	3	1	2	1	2	NI
16[a]	2	3	1	2	1	2	1•	3	1	CI
17[a]	2	3	1	2	2	3	1	1	2	CI
18	2	3	1	2	3	1	2	2	3	PI
19[a]	3	1	3	2	1	3	2	1	3	CI
20	3	1	3	2	2	1	1•	2	1	NI
21	3	1	3	2	3	2	1	3	2	NI
22[a]	3	2	1	3	1	3	2	2	1	CI
23	3	2	1	3	2	1	1•	3	2	NI
24	3	2	1	3	3	2	1	1	3	NI
25	3	3	2	1	1	3	2	3	2	CI
26	3	3	2	1	2	1	1•	1	3	NI
27	3	3	2	1	3	2	1	2	1	CI

A: Temperature.
B: Time.
C: Temp. × Time.
D: Particle Size.
E: Porosity.
NI: Not Infiltrated.
F: Phase of SiO_2.
G: Alloy.
H: Porosity × Time.
I: SiO_2 content.
PI: Partially Infiltrated.
CI: Complete Infiltration.
[a] Those which were effloresced after infiltration process within one or two weeks.

Table 1
Parameters and levels tested for Al/SiC/RHA composites fabrication.

Parameters	Level 1	Level 2	Level 3
Temp.	1100 °C	1200 °C	1300 °C
Time	90 min	120 min	150 min
Particle Size	10 μm/129 μm	129 μm/10 μm	mixture/mixture
Porosity of preform	40%/60%	60%/40%	50%/50%
SiO_2 crystallinity	Crystal (Type I)	Amorphous	Crystal (Type II)
Alloy	Alloy 1 (Low Mg)	Alloy 2 (High Mg)	
SiO_2 content	10 wt%	15 wt%	20 wt%
Interaction 1	Temperature × Time		
Interaction 2	Porosity × Time		
Constants	• Rate of N_2: 30 cm^3/min	• Amount of alloy: 20g	• Size of preforms and layers

(including extraction and re-insertion of the specimen in the measurement rig); the variation of the data was found to be in the order of 0.1% of the mean value.

The thermal diffusivity (α) was measured by the laser flash method on square or disk samples of dimensions 8 × 8 × 1 mm and 10 × 1 mm, respectively, using a Netzsch LFA 457 MicroFlash™ diffusivity apparatus. The surfaces of the samples were graphite coated to avoid direct transmission of the laser pulse through the specimen and to improve energy absorption. Measurements were done from room temperature up to 300 °C always in an argon atmosphere.

3. Results and discussions

The microstructures of the all fabricated Al/SiC/RHA bilayer composites studied in this work have previously been studied by scanning electron microscopy and X-ray diffraction [10]. Both layer of composite fabricated according to L2 configuration as well as microstructure of bilayer L17 are presented in Fig. 1a–c. SEM and XRD analyses confirmed that during pressureless infiltration of aluminum alloys into SiC/RHA porous preforms, RHA keeps its structure, and depending on the crystallinity of RHA (crystalline or amorphous), it acts as an oxygen donator to form $MgAl_2O_4$ and MgO. Moreover, it prevents formation of the deleterious phase, aluminum carbide in compliance with Le Chatelier's principle. Also, formation of AlN was intensified when high infiltration temperature (1300 °C) and long processing time (150 min) were used for fabrication of Al/SiC/RHA composites. As it can be seen in Fig. 1a and b, complete infiltration caused a microstructure free of defects such as porosity, cracks and inhomogeneity. Short infiltration time or low processing temperature as well as inappropriateness of preform architecture can cause incomplete infiltration in top layer of preform or free metal regions in the final microstructure of obtained composite (Fig. 1c).

3.1. Bending strength and modulus of elasticity (from bending test and ultrasonic method) of Al/SiC/RHA bilayer composites

Typical stress–strain curves recorded during the four-point bending test of bilayer and monolayer Al/SiC/RHA composites are shown in Fig. 2. Also, the value of modulus of elasticity calculated from both pulse-echo ultrasonic method and stress-strain curves as well as bending strength of both monolayers and bilayer composites, are presented in Table 3. As it can be seen from Fig. 2, the plastic deformation zone is disappeared due to brittle essence of ceramic particles and as a consequence MMCs with high percentage of ceramic reinforcements.

It is clear from Fig. 2 that except for L9-Al/SiC/RHA composite, each layer of bilayer composite, depend on the weight percentage of reinforcement and the position of layer (bottom or top) during pressureless infiltration process has different bending strength from another layer and bilayer composite. Also, it can be observed that L27 bilayer composite has the highest bending strength (334 MPa), followed by L25 (298 MPa) and L8 (271 MPa) composite. Considering the L27 Taguchi table, amorphous RHA was used in both L27 and L8 composite. High temperature and long process time (L25 and L27) cause complete formation of hard phases such as AlN and $MgAl_2O_4$ through the matrix. Also, L8 configuration provides the situation that high Mg alloy is in contact with amorphous RHA for a long procedure time. It causes formation of MgO in addition to $MgAl_2O_4$ and AlN in matrix.

In addition to chemical composition of composite, the reinforcement architecture could be other important factor which controls the crack nucleation and propagation through the layers. Load bearing layer of both L27 and L8-Al/SiC/RHA which have highest bending strength values, contains small size particle of SiC with almost low level of preform porosity. Since there is a good bonding between matrix and particle, the crack initiation site would be limited.

As it can be seen from Fig. 2 and Table 3, in general it can be said that those composite who their load bearing layer has higher bending strength than another layer, have higher total bending strength (Such as L27, L25, L13 and L2). Comparison between young's modulus data obtained by Pulse-Echo technique and from stress-strain curves shows that there is a negligible difference between the results obtained by these two methods. It can arise from difference between the tested areas in the samples. Probe in Pulse-Echo method covers an area of 0.78 cm^2 while bending sample fabricated according to configuration A of ASTM 1161 standard covers an area of 0.4 cm^2. The fracture micrographs of monolayer and bilayer L27 Al/SiC/RHA composite are presented in Fig. 3. It clearly shows that almost all the SiC particles on the fracture surfaces belong to the cracked particles rather than debonded ones and the most of particles run parallel to the fracture surfaces of the composites.

This mode of fracture indicates that the failure is dominantly caused by the SiC particles fracture and Al-matrix dimple rapture rather than by the interface debonding, which means that the interface bonding between Al-matrix and SiC reinforcement is significantly strong. Interface bonding as well as fine aluminum dimples and cleavage fragment of SiC particle can be seen clearly in Fig. 4.

Also, magnesium in the aluminum alloy can reduce the oxides present in the preform systems due to its high affinity for oxygen; thus, development of the magnesium aluminate spinel ($MgAl_2O_4$) during the processing is highly feasible (see Fig. 3). As it was reported before, reduction of SiO_2 by molten aluminum and magnesium occurs through extremely exothermic events. The spontaneity of this reaction through the whole range of temperatures fairly explains the presence of $MgAl_2O_4$ in mostly all

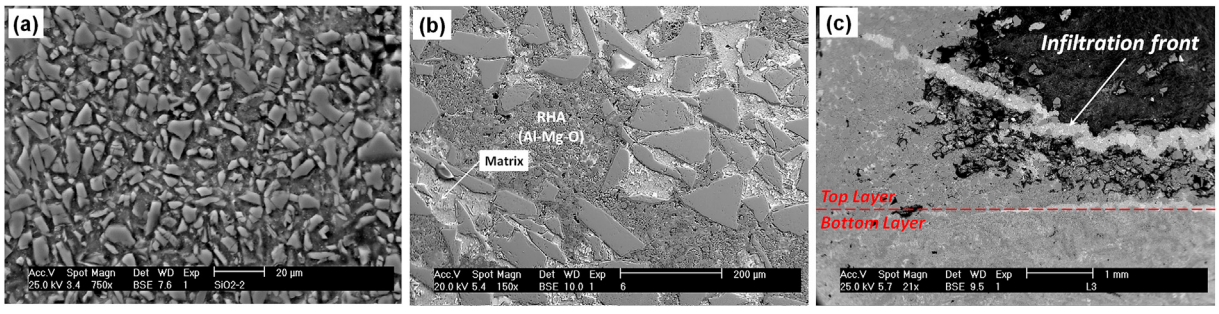

Fig. 1. SEM micrograph of a) and b) both layer of L2 Al/SiC/RHA composite and c) L17 bilayer Al/SiC/RHA composite.

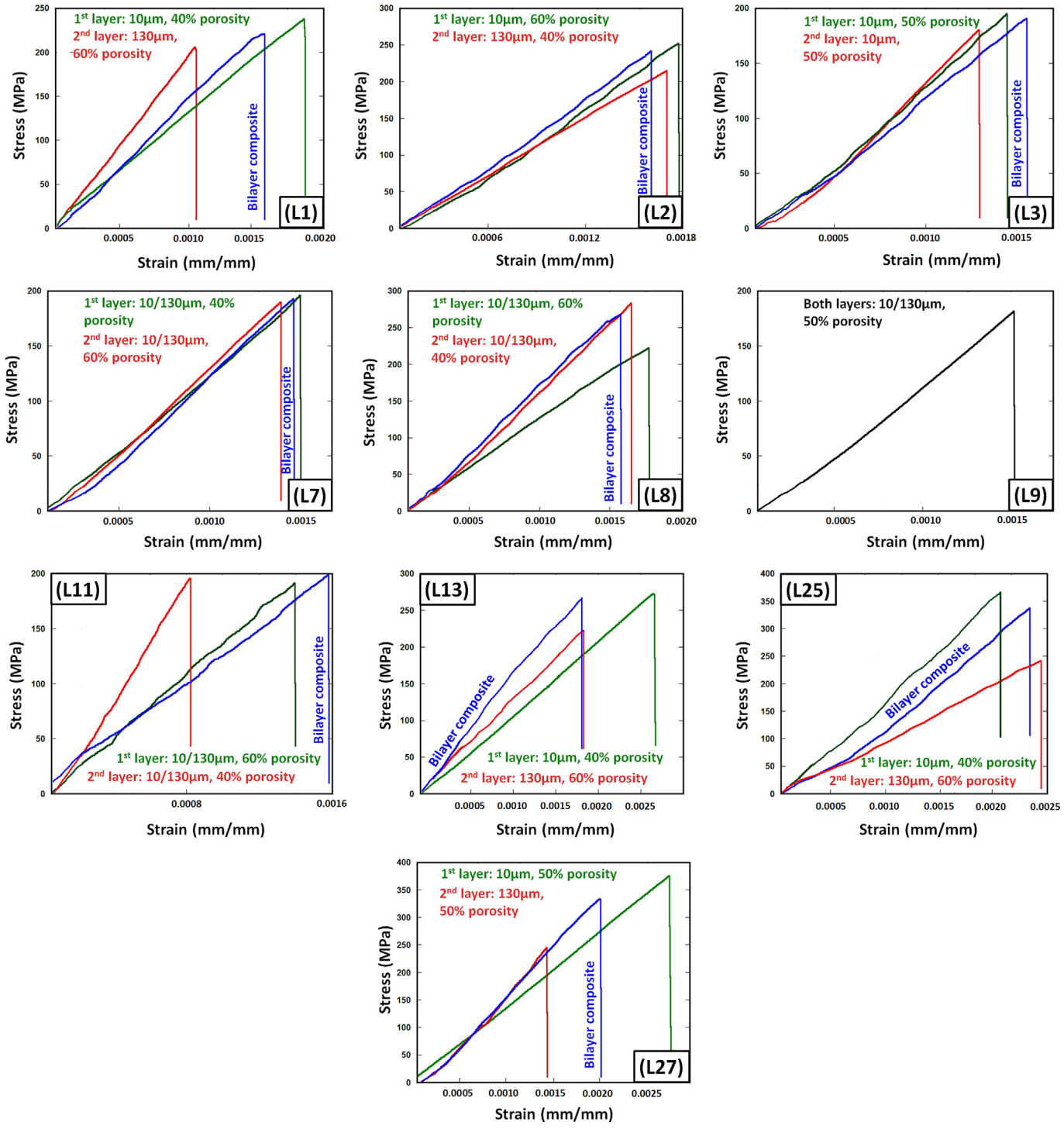

Fig. 2. Typical stress–strain curves recorded during the four-point bending test of bilayer and monolayer Al/SiC/RHA composites.

fabricated composites.

AlN fine needles can be observed in all examined fracture surface of Al/SiC/RHA composites. Aluminum nitride (AlN) may be produced through the direct reaction of molten aluminum and nitrogen gas according to [17]:

$$Al\ (l) + [N] \rightarrow AlN\ (s) \qquad \Delta G^{\circ}_{1100} = -556.2\ \text{kJ/mol} \tag{1}$$

However, due to the presence of magnesium in the system, AlN can be formed through the following reactions as well:

$$3Mg\ (g) + 2\ [N] \rightarrow Mg_3N_2\ (s) \qquad \Delta G^{\circ}_{1100} = -945.5\ \text{kJ/mol} \tag{2}$$

$$Mg_3N_2\ (s) + 2Al\ (l) \rightarrow 2AlN\ (s) + 3Mg\ (l) \qquad \Delta G^{\circ}_{1100} = -166.3\ \text{kJ/mol} \tag{3}$$

Reaction 2 implies the interaction of Mg in vapor phase with the flowing nitrogen in the process atmosphere. In order to take

Table 3
Young's modulus (calculated by pulse-echo ultrasonic method and stress-strain curve) and bending strength of Al/SiC/RHA monolayer and bilayer composites.

Sample		Young's modulus (GPa) (pulse-echo ultrasonic determination)	Young's modulus (GPa) (Stress-strain curve)	Bending strength (MPa)
L1	1st Layer	118.12	113.16	240
	2nd Layer	135.24	142.31	205
	Bilayer	124.36	121.21	220
L2	1st Layer	131.58	127.37	251
	2nd Layer	110.34	106.25	212
	Bilayer	128.61	125.17	245
L3	1st Layer	111.30	115.86	195
	2nd Layer	120.68	117.65	183
	Bilayer	105.43	106.54	190
L7	1st Layer	112.39	113.08	198
	2nd Layer	116.10	115.07	180
	Bilayer	114.47	117.02	196
L8	1st Layer	105.26	102.63	220
	2nd Layer	136.74	139.20	286
	Bilayer	135.37	130.29	268
L9		105.61	103.43	182
L11	1st Layer	117.58	119.29	192
	2nd Layer	140.23	148.66	197
	Bilayer	116.49	113.51	200
L13	1st Layer	126.21	122.54	276
	2nd Layer	101.89	106.77	225
	Bilayer	129.35	132.99	270
L25	1st Layer	162.67	159.62	360
	2nd Layer	94.45	89.92	243
	Bilayer	134.12	129.37	335
L27	1st Layer	160.27	156.68	380
	2nd Layer	119.69	122.25	248
	Bilayer	163.91	160.80	340

advantage of magnesium as a surfactant element and thus enhance the wetting of the ceramic reinforcement by liquid aluminum, it is highly desirable that reactions 2 and 3 take place. In this way, Mg is recycled to the melt [18]. Due to its low vaporization temperature as compared to that for aluminum at normal pressure, magnesium escapes from the melt during processing. Reactions 2 and 3 are strongly exothermic and although from the thermodynamics standpoint, nitridation of both, Mg and Al is highly feasible, according to the literature, kinetically the reaction for formation of Mg_3N_2 is much more favorable than that for AlN. In the present work, aluminum nitride was typically observed in the microstructure of the composite nearby the metal/ceramic interface in the form of needles or fibers oriented randomly, as illustrated in Fig. 5.

Fig. 6 shows the fracture surface of L3-Al/SiC/RHA composite. As it can be seen, there exist alloy free zones in fracture surface of both layers of fabricated composite. It can be attributed to the poor wettability of SiC/20 wt% RHA mixture with low mg alloy at low processing temperature. Also, the nucleus of AlN in both layers were observed on SiC particles, indicating that the situation provided by configuration L3 were not adequate enough to intensify the growth of AlN fibers or needles.

Analysis of variance (ANOVA) was performed on the data in order to identify the effect of each parameter and each interaction on the modulus of elasticity and bending strength of the graded composites. Results of the pooled ANOVA for the modulus of elasticity are shown in Table 4. This table indicates that, at the levels studied, the parameter that affects the bending strength of graded composites most significantly is temperature of infiltration process followed by interaction of time and temperature of process and chemical composition of alloy. Their relative contribution to the variance in the modulus of elasticity values are 32, 14 and 13%, respectively. Temperature and time of process can define the amount of matrix free regions and consequently the retained porosity content of fabricated composite.

Considering the parameters and levels of designed experiment, the maximum bending strength can be obtained by using the process parameters shown in Table 5. When using these process parameters, the projected bending strength is 363 ± 5 MPa.

Results of the pooled ANOVA for the modulus of elasticity calculated from echo-pulse ultrasonic method are shown in Table 6. This table indicates that, at the levels studied, the parameter that affects the modulus of elasticity of graded composites most significantly is time of process. Its relative contribution to the variance in the modulus of elasticity values is 27%. It is expected that, due to capillary effects, this parameter has a significant contribution to the modulus of elasticity values because an inadequate time may restrict the elevation of the liquid metal up to the interface formed by both preforms and end of the preforms and causes high percentage of porosity content. The residual porosity in the composites negatively affects the wave velocity because wave propagation is higher in solids than in air. SiO_2 crystallinity, on the other hand has a direct effect on the level of in-situ formed phases in the final composite and as a result can affect the density of fabricated composites and their modulus of elasticity values. Preform porosity, also affects the modulus of elasticity of the composites notably. Its relative contribution to the modulus of elasticity is about 13%. It is expected that the original porosity designed in the preform has a relatively high effect on the composite's modulus of elasticity since this porosity becomes infiltrated with the less elastic component of the composite, i.e. aluminum alloy. Consequently, the higher the preform porosity levels, the higher the aluminum alloy content of the composite, and the lower the modulus of elasticity of the composite. The percent contribution due to the error term in this ANOVA is 1%. This indicates that no important factors were omitted in the design of the experiment, and measurement errors were trivial.

Considering only the parameters and interactions included in Table 1 in the ranges tested, the maximum modulus of elasticity can be obtained by using the process parameters shown in Table 7. When using these process parameters, the projected modulus of elasticity is 169 ± 9 GPa.

Table 8 lists the results of the pooled ANOVA for the modulus of

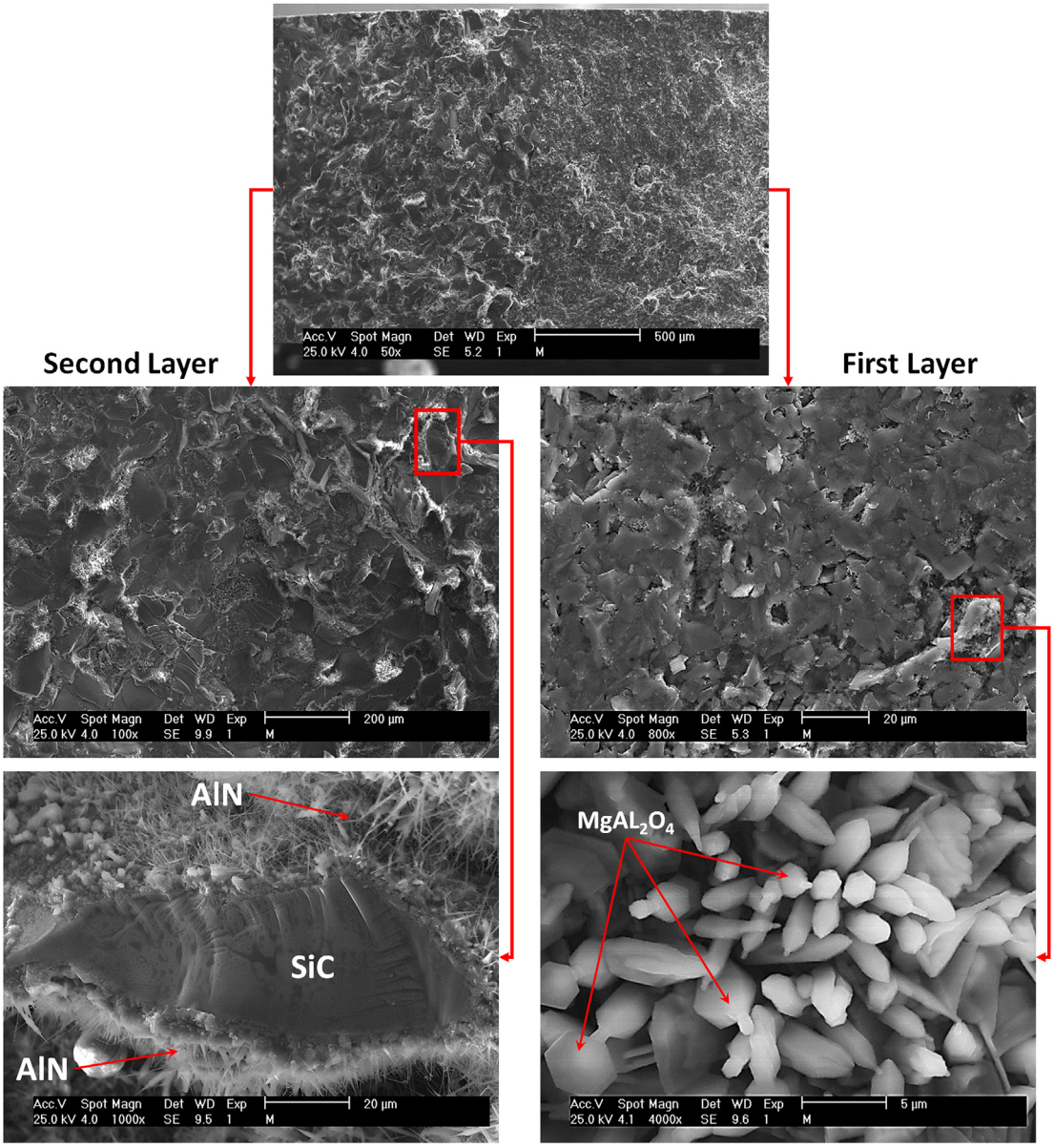

Fig. 3. The fracture micrographs of monolayer and bilayer L27 - Al/SiC/RHA composites.

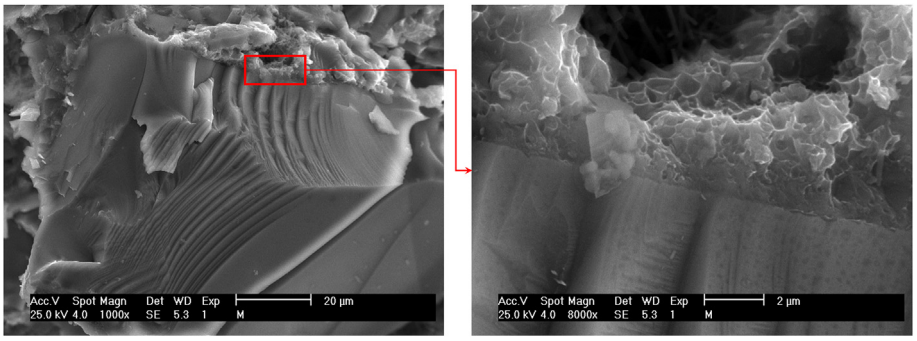

Fig. 4. Good bonding between SiC particles and matrix alloy.

elasticity obtained from stress-stress curves. Table 8 indicates that, at the levels studied, the parameter that affects the modulus of elasticity of graded composites most significantly is time of process. Its relative contribution to the variance in the modulus of elasticity

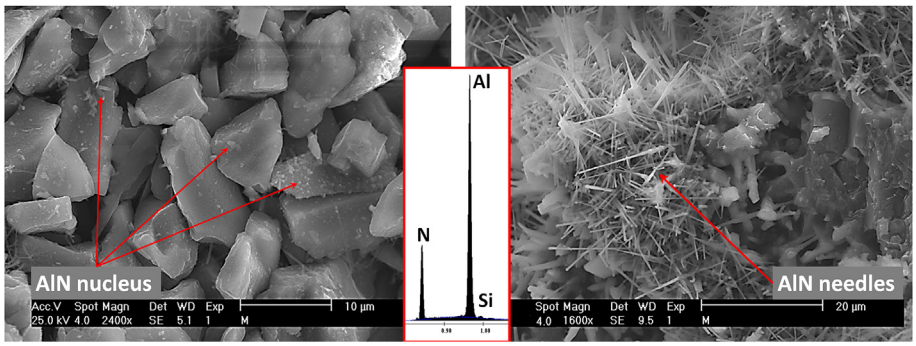

Fig. 5. Presence of AlN needles in fracture surface of Al/SiC/RHA composite.

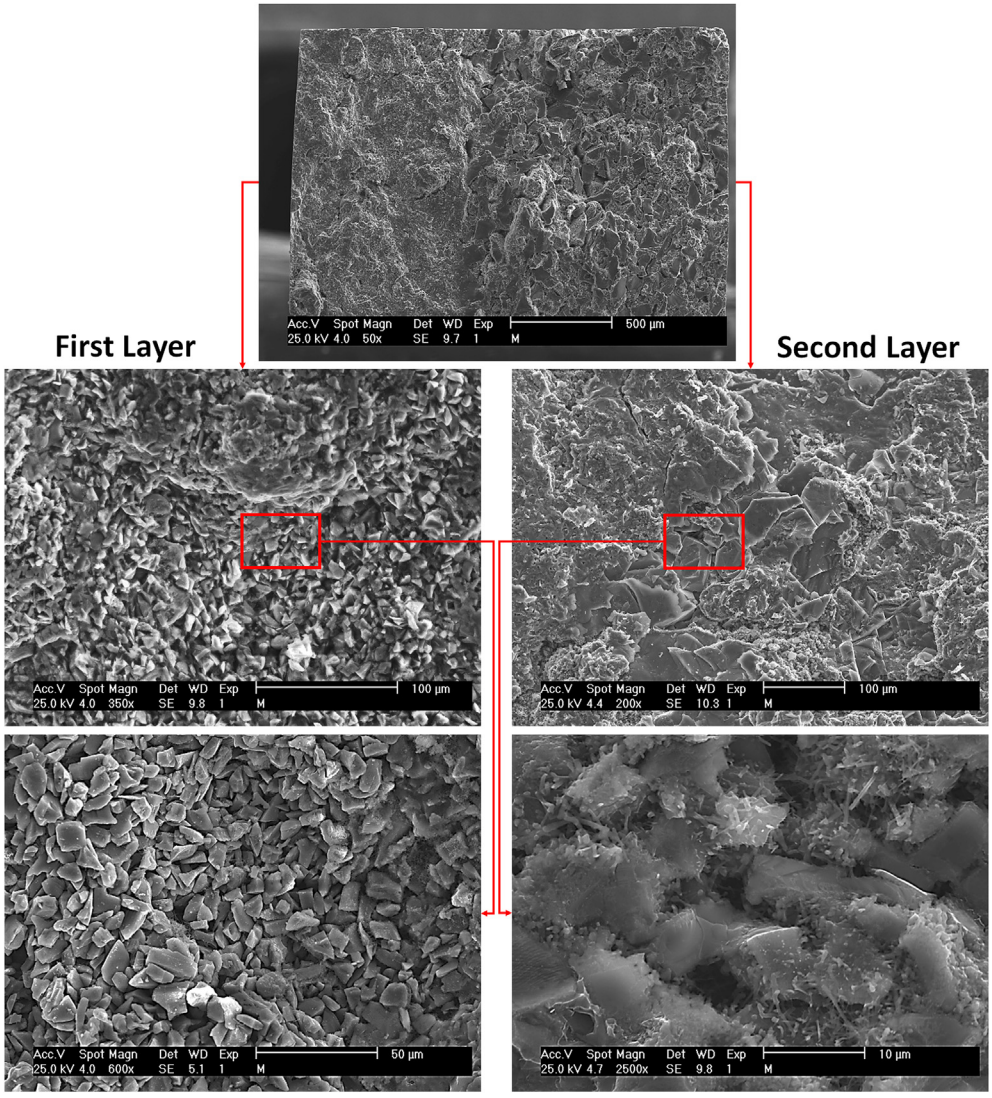

Fig. 6. The fracture micrographs of monolayer and bilayer L3 - Al/SiC/RHA composites.

values is 27%.

Considering only the parameters and interactions included in Table 1 in the ranges tested, the maximum modulus of elasticity can be obtained by using the process parameters shown in Table 9. When using these process parameters, the projected modulus of elasticity is 173 ± 6 GPa.

Since both sets of processing parameters — obtained through ANOVA — for maximum bending strength and modulus of elasticity obtained from both methods of pulse-echo ultrasonic method and stress-strain curves are the same, they were validated in one single verification test under the experimental conditions established in Tables 5, 7 and 9. The fact that all optimum processing parameter

Table 4
Pooled ANOVA table for maximum bending strength of Al/SiC/RHA graded composite.

Column	Factors	Sum of squares	Variance	Contribution percentage
1	Temperature	22071	11035	32
2	Time	6372	3186	9
3	Temperature × Time	9689	4844	14
4	Particle size	7304	3652	10
5	Porosity of preform	756	Pooled	Pooled
6	Alloy	9180	4590	13
7	Porosity × Time	6210	6210	9
8	SiO_2 Content	94	Pooled	Pooled
9	Phase of SiO_2	6968	3484	10
Error		2E+03		3
Total		6.86E+04		

Table 5
Optimum process parameters for maximum bending strength of Al/SiC/RHA graded composite.

Parameters	Proposed levels
Temperature (°C)	1100
Time (min)	150
Particle size (μm)	10 μm/129 μm
Porosity (%)	40-60n m
Phase of SiO_2	Amorphous
Alloy	High Mg
SiO_2 content (wt%)	10

Table 7
Optimum process parameters for maximum modulus of elasticity (Obtained from pulse-echo ultrasonic method).

Parameters	Proposed levels
Temperature (°C)	1100
Time (min)	150
Particle size (μm)	10–129
Porosity (%)	40–60
Phase of SiO_2	Amorphous
Alloy	High Mg
SiO_2 content (wt.%)	10

sets obtained in separate ANOVA tables are the same, provides an increased level of confidence in the obtained results. The measured modulus of elasticity calculated by pulse-echo ultrasonic method and from stress-strain curve are 165 and 170 GPa, respectively, and the determined bending strength 369 MPa. These results are in good agreement with the projected values (169 ± 9, 173 ± 6 GPa and 363 ± 5 MPa, respectively).

3.2. Thermomechanical analyzes

3.2.1. Aluminum alloys and rice husk ash

The dimensional and mechanical stability of materials is of paramount importance to their use in the everyday world where they may encounter a wide variation in temperature through design or by accident. Fig. 7 shows thermal strain response curve obtained during heating and cooling of amorphous silica and crystalline silica. In crystalline silica, a considerable increase and decrease were observed during heating and cooling of sample, respectively. It can be attributed to the phase transformation of cristobalite $\alpha \rightarrow \beta$. This behavior is in good agreement with previous works [19,20]. Also, this phase transformation is confirmed by DTA results presented in Fig. 8. As it can be seen, a sharp increase and decrease in both heating and cooling curves of amorphous silica were observed at temperature of about 200 °C. According to Huang and Kieffer [21], thermomechanical anomalies of amorphous silica are due to the localized reversible structural transitions, which are facilitated by modes of atomic displacement similar to the ones underlying the $\alpha \rightarrow \beta$ cristobalite phase transformations in crystalline silica, i.e., spontaneous Si-O-Si bond rotations. This phenomenon also is confirmed by DTA and TG results obtained from heating of amorphous rice husk ash (Fig. 8). It was also reported that the thermal expansion of amorphous silica is much lower than that of silicon. In contrast, the thermal expansion of crystalline silica is higher than that of silicon [22].

Fig. 9 shows thermal strain response curve obtained during the four cycles of heating and cooling between 25 °C and 250 °C on pure aluminum, alloy 1 and 2. Also CTE values of alloys in different temperature for each heating curves are presented in Fig. 9. As it can be seen, alloying causes a decrease in the CTE value of pure aluminum. Higher level of Mg in Alloy 2 increase the percentage of Mg_2Si intermetallic (CTE: 7.5×10^{-6}/°C) in the alloy and as a consequence more reduction in CTE value of alloy 2 in comparison to alloy 1. CTE of Al-matrix (aluminum alloys) increased with the increasing temperature. The average distance between α (Al) atoms in crystal lattice was enlarged by the intensified lattice vibration, which impaired the metallic bonds and elastic modulus and finally

Table 6
Pooled ANOVA table for maximum modulus of elasticity (Obtained from pulse-echo ultrasonic method).

Column	Factors	Sum of squares	Variance	Contribution percentage
1	Time	19176.52	9588.26	27
2	Phase of SiO_2	15254.61	7627.30	21
3	Porosity	9455.42	4727.71	13
4	Temperature × Time	1508.18	377.04	2
5	Particle Size	786.55	786.55	1
6	Temperature	7850.57	3925.28	11
7	Alloy	8462.21	4231.10	12
8	Porosity × Time	3399.94	849.99	5
9	SiO_2 Content	5056.66	2528.33	7
Error		520.64	16.27	1
Total		71471.30		100

Table 8
Pooled ANOVA table for maximum modulus of elasticity (obtained from stress-strain curve).

Column	Factors	Sum of squares	Variance	Contribution percentage
1	Temperature	775	387	4
2	Time	13295	6647	68
3	Temperature × Time	386	193	2
4	Particle size	8.8	Pooled	Pooled
5	Porosity of preform	1161	580	6
6	Alloy	1222	611	6
7	Porosity × Time	77	Pooled	Pooled
8	SiO_2 Content	177	Pooled	Pooled
9	Phase of SiO_2	423	211	8
Error		1.14E+03		6
Total		1.94E+04		

Table 9
Projected process parameters for maximum modulus of elasticity (obtained from stress-strain curve).

Parameters	Proposed levels
Temperature (°C)	1100
Time (min)	150
Particle size (μm)	10 μm/129 μm
Porosity (%)	40–60
Phase of SiO_2	Amorphous
Alloy	High Mg
SiO_2 content (wt%)	10

resulted in the growth of CTE. However, it was reported that CTE of Al-Mg-Si alloys slightly fell down when temperature was higher than 400 °C. This deregulation could be explained by the increasing solubility of silicon and magnesium in α (Al) crystal at high temperatures, which reduced the lattice constant of α (Al) crystal [23]. The thermal response curves illustrate how the material expands and contracts in response to fluctuations in the operating temperature. Three parameters commonly used to characterize these curves are shown also in Fig. 9. The ε^p is used to quantify the residual plastic strain, $\Delta\varepsilon^t$ is used to quantify the largest vertical (at a given temperature) difference between the cooling and heating curves, and ε^c is the cyclic strain which gives information equivalent to that provided by the CTE. The degree of thermal damage and stability can be evaluated from ε^p, $\Delta\varepsilon^t$ and ε^c.

The thermal response results of all specimens from the heating of the first cycle to the cooling of the forth cycle are shown in Table 10. The results show that the ε^p and ε^c of all samples decreased as the percentage of alloying elements increased, indicating that Si and Mg addition to the aluminum is beneficial to the dimensional stability of Al-Mg-Si alloy.

3.2.2. Al/SiC/RHA bilayer composite

CTE values obtained from thermal strain response curves of all fabricated Al/SiC/RHA composites are presented in Fig. 10. It is clear that addition of reinforcing phases to Al-Si-Mg alloys leads to a dramatic decrease in the value of CTE. The thermal response results of all fabricated composites from the heating of the first cycle to the cooling of the forth cycle are shown in Table 11. As it can be seen, lowest parameters (ε^p, ε^c and $\Delta\varepsilon^t$) are belonged to the samples with low CTE values. Thermal strain can be attributed to thermal stress. During heating process, the thermal stress exhibit as tensile stress on the ceramic reinforcement and compressive stress on the metal matrix. On the contrary, during cooling process the thermal residual stresses exhibit as compressive stress on ceramic reinforcement and tensile stress on the metal matrix. Assumed that both elastic and plastic deformation form as the thermal strain response,

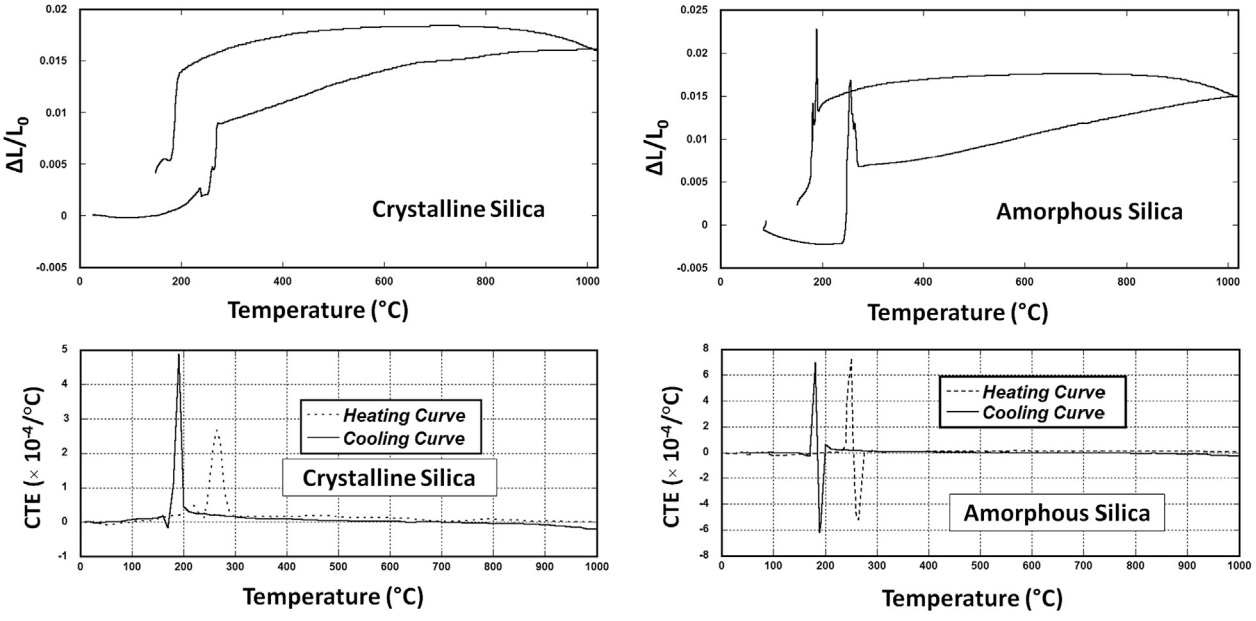

Fig. 7. Variation of $\Delta L/L_0$ and CTE values vs. temperature for crystalline and amorphous silica derived from rice husk.

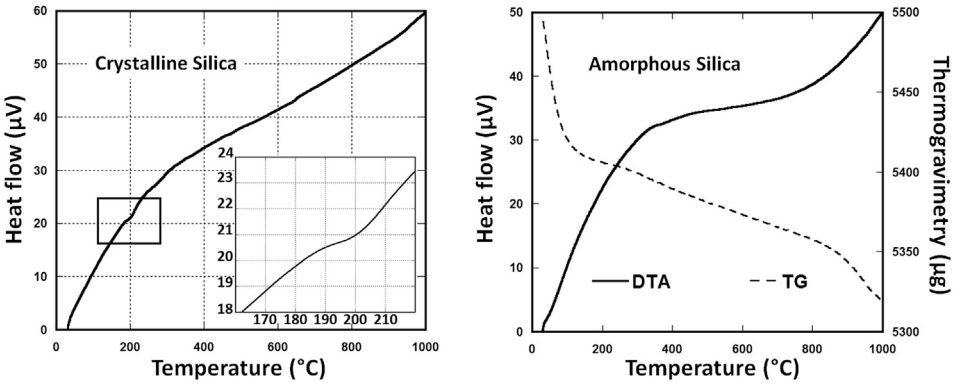

Fig. 8. Heat flow curves for crystalline and amorphous silica.

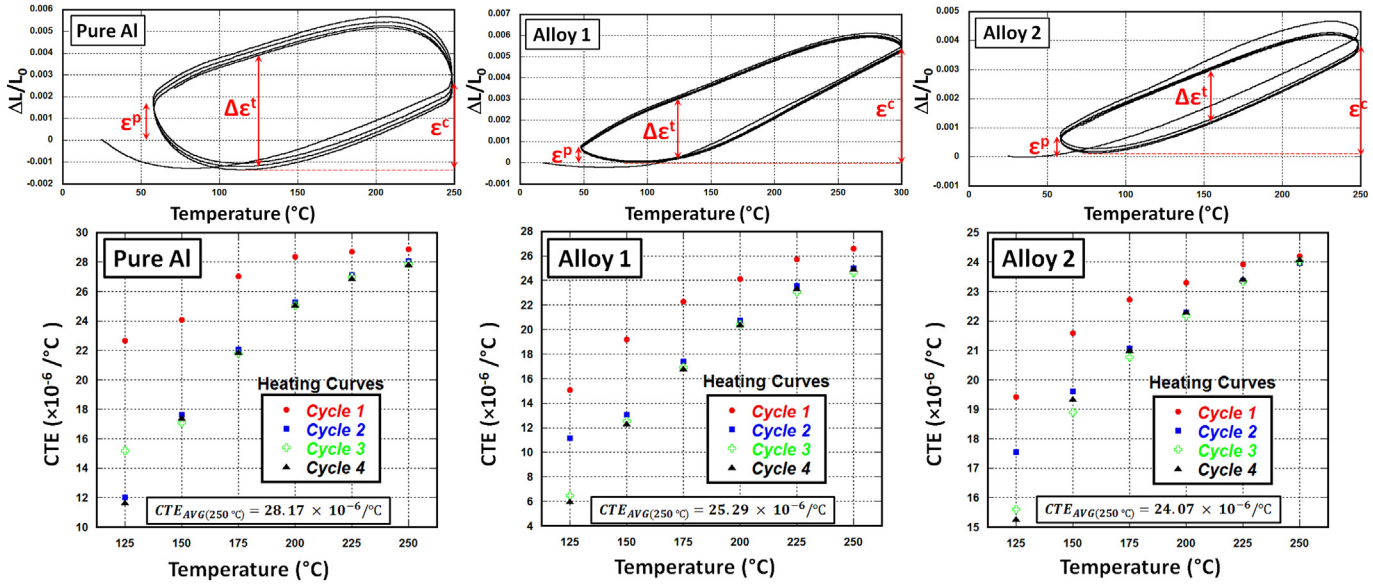

Fig. 9. Thermal strain response curve and CTE values obtained during the four cycles of heating and cooling between 25 °C and 250 °C on pure aluminum, alloy 1 and 2.

Table 10
Thermal response parameters and CTE of pure aluminum and Al-Mg-Si alloys with different content of Mg.

Materials	ε^p	ε^c	$\Delta\varepsilon^t$	CTE (10^{-6}/°C)
Pure Al	0.00087	0.0030	0.0054	28.17
Alloy 1	0.00068	0.0050	0.0038	25.29
Alloy 2	0.00062	0.0048	0.0030	24.07

the elastic displacements are recovered during cooling. Therefore, higher thermal stress can lead to the generation of strain hysteresis between the heating and cooling cycles and to the retention of residual strain as the result of the plastic deformation or yielding of materials [24]. The thermal hysteresis behavior can be explained in terms of the weak interface between reinforcements and matrix or large internal stress released in the composites. Once the composite had undergone significant plastic deformation during the heating process, the lack of bonding force could not produce large enough stress to deform the matrix back to its original size upon cooling.

It is generally known that thermal stress results from thermal expansion incompatibility in materials during the temperature changes. Such a stress can induce the thermal strain in the specimens during thermal cycling. High thermal stress can lead to the generation of strain hysteresis between the heating and cooling cycles and to the retention of residual strain. The residual strain is the result of the plastic deformation or yielding of the materials. The origins of thermal stress include thermomechanical mismatch between two materials, non-uniform temperature distribution in a material and thermal expansion anisotropy in a single phase material [25]. In the case of MMCs, thermal stress is known to arise from the difference of the CTE values between the matrix and ceramic reinforcing phase.

Pooled ANOVA results for the CTE values of Al/SiC/RHA graded composite are listed in Table 12. It shows that at the levels studied, the parameter that affects the CTE values of composite most significantly is the temperature of infiltration process. Its relative contribution to the variance in composite CTE value is 28%. Time of infiltration process and interaction of time and temperature have the same effect on the CTE values of composite with the contribution percentage of 16%. As it was discussed before temperature of process can define the amount of new ceramic phases in final structure of composite. From the data, which are presented in Table 12 it can be concluded that the composites which were made in higher processing temperature have lower CTE values than those were fabricated in lower temperature.

Considering experiment parameters and levels designed for this

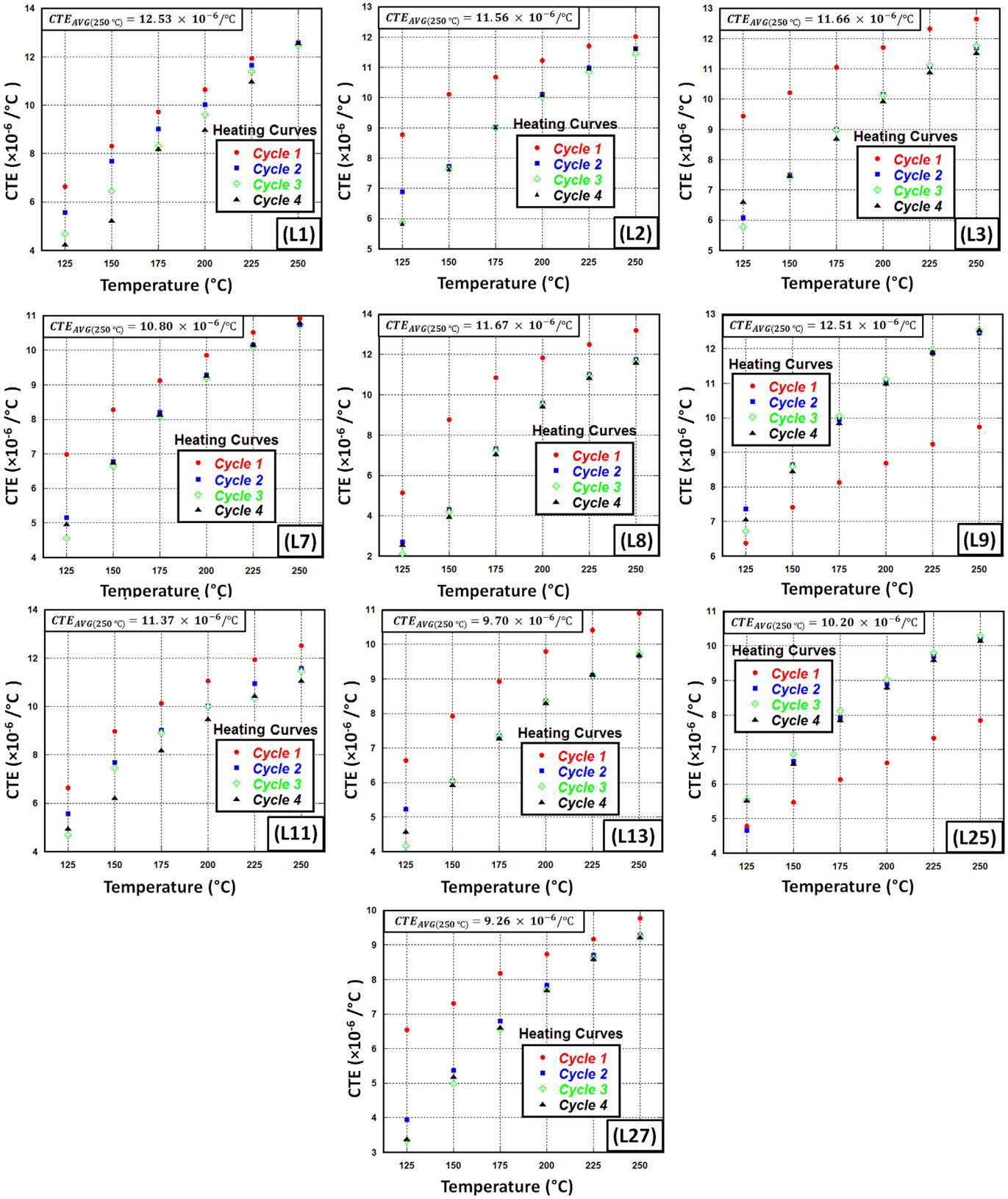

Fig. 10. CTE values obtained during the four cycles of heating and cooling between 25 °C and 250 °C on Al/SiC/RHA composites.

study, the minimum CTE value can be obtained by using the process parameters shown in Table 13. When using these process parameters, the projected CTE value is $8.6 \pm 1.2 \times 10^{-6}/°C$.

The verification test has been done according to the optimum parameters proposed by ANOVA for minimum CTE value. The measured CTE was $8.9 \pm 0.8 \times 10^{-6}/°C$. This result is in good

Table 11
CTE values calculated from heating curves of thermal strain response curve of Al/SiC/RHA composites, obtained during the four cycles of heating and cooling.

Composites	ε^p	ε^c	$\Delta\varepsilon^t$ (10^{-3})	*CTE* (10^{-6}/°C)
L1	0.0008154	0.001904	2.015	12.53
L2	0.0007632	0.001868	1.588	11.56
L3	0.0006390	0.001706	1.610	11.66
L7	0.0005089	0.001413	1.547	10.80
L8	0.0003174	0.001114	1.996	11.67
L9	0.0008025	0.001882	1.706	12.51
L11	0.0007293	0.001822	1.590	11.37
L13	0.0005696	0.001368	1.466	9.70
L25	0.0007504	0.000977	1.440	10.20
L27	0.0005346	0.001132	1.467	9.26

agreement with the projected values ($8.6 \pm 1.2 \times 10^{-6}$/°C).

3.3. Electrical resistivity

Electrical resistivity and conductivity were measured using four-point probe technique on the flat faces of the samples. Fig. 11 shows those values for pure aluminum, alloy 1 and alloy 2. As it can be seen alloying with Mg and Si cause a reduction in electrical conductivity of pure aluminum. Reduced conductivity in solid solutions is explained as follows. Atoms of the two metals concerned, having a certain resemblance, enter side by side into the same crystal lattice. Hence, a mixed crystal is formed. In this new distorted structure, the electrons find difficulty in moving from atom to atom. Thus the resistance of the alloy becomes greater [26]. Furthermore, this reduction was intensified by increasing Mg content in alloy 2 due to formation of intermetallic phase of Mg_2Si (electrical conductivity of $Mg_2Si = 14 \times 10^2\ \Omega^{-1}m^{-1}$) [27].

Fig. 12 shows the electrical resistivity and conductivity of all monolayer and bilayer Al/SiC/RHA fabricated composites. As it can be seen among Al/SiC/RHA bilayer fabricated composites, L27 composite has the highest resistivity ($2.02 \times 10^{-3}\ \Omega$ m) and lowest conductivity ($4.95 \times 10^2\ \Omega^{-1}\ m^{-1}$) values. Since in all fabricated composites, in addition to the main constituents, secondary phases (MgO, $MgAl_2O_4$, AlN, Al_4C_3, etc.) are formed, their electrical properties can affect the final properties of composite positively or negatively.

Aluminum nitride (AlN) ceramics are currently of interest because they combine a high thermal conductivity (175 W/mK) with a high electrical resistance ($>10^{12}\ \Omega$ m) at room temperature. As it was reported before [10], formation of AlN in Al/SiC/RHA composites were confirmed by XRD and EDS. The amount of AlN phase in the final fabricated composite is controlled by different parameters, such as Mg concentration of alloy, time and temperature of infiltration process etc. In XRD pattern of L27-Al/SiC/RHA composite, intensity of AlN peaks are stronger than those of other composites [10]. Therefore, high electrical resistivity of L27-Al/SiC/RHA composite could be attributed to the formation of high amount of AlN during fabrication process.

Table 13
Optimum process parameters for minimum CTE value of Al/SiC/RHA composite.

Parameters	Proposed levels
Temperature (°C)	1300
Time (min)	120
Particle size (μm)	mixture/mixture
Porosity (%)	50–50
Phase of SiO_2	Crystal (Type I)
Alloy	Low Mg
SiO_2 content (wt%)	10

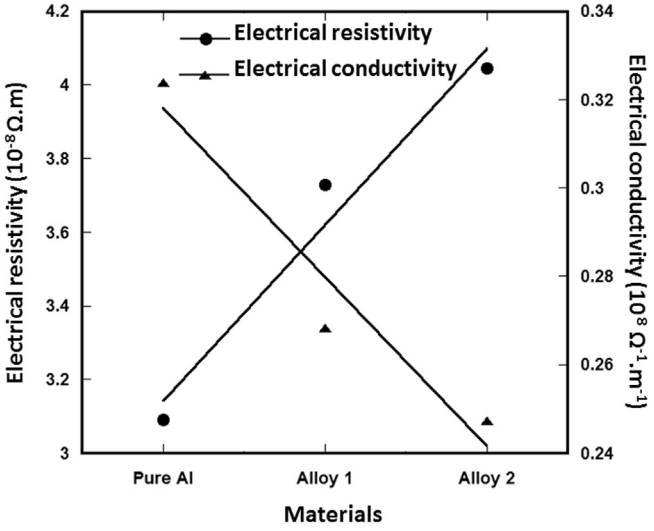

Fig. 11. Electrical conductivity and resistivity of pure aluminum, alloy 1 and alloy 2.

Besides AlN, other ceramic phase that can have direct effect on electrical properties of Al/SiC/RHA composite is $MgAl_2O_4$. $MgAl_2O_4$ exhibits a unique combination of properties such as a low thermal conductivity, a low coefficient of thermal expansion, good thermal shock resistance, a low dielectric constant and high electric resistivity ($0.83 \times 10^{-2}\ \Omega$ m) [28]. Like AlN, formation of $MgAl_2O_4$ is highly depended to the temperature of process and crystallinity of RHA as an oxygen donor during the fabrication processing. L27 configuration provides a condition with high processing temperature for transformation of MgO phase to $MgAl_2O_4$ and also amorphous RHA with high reactivity and suitable structure for oxygen donation.

Table 12
Pooled ANOVA table for minimum CTE value of Al/SiC/RHA composites.

Column	Factors	Sum of squares	Variance	Contribution percentage
1	Temperature	7.2	3.6	28
2	Time	4	2	16
3	Temperature × Time	4	2	16
4	Particle Size	1.4	0.35	5
5	Porosity	0.9	0.45	3
6	Alloy	2.3	1.15	9
7	Porosity × Time	0.0012	Pooled	Pooled
8	SiO_2 Content	2.3	1.15	9
9	Phase of SiO_2	0.5	0.25	9
Error		1.26		5
Total		2.52E+01		

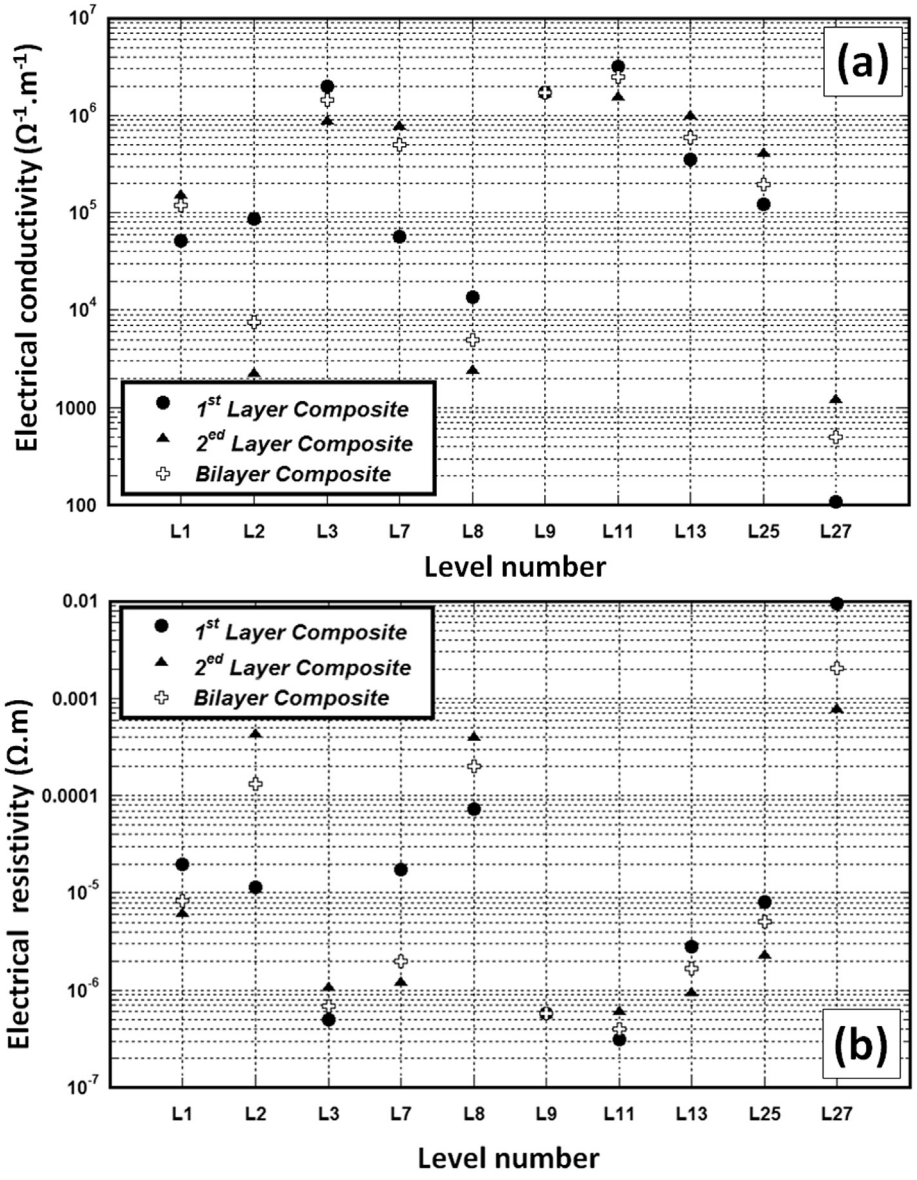

Fig. 12. Electrical a) conductivity and, b) resistivity of monolayer and bilayer Al/SiC/RHA fabricated composites.

Analysis of variance (ANOVA) was performed on the data in order to identify the effect of each parameter on the electrical resistivity of the graded composites. Results of the pooled ANOVA for the electrical resistivity are shown in Table 14. This table indicates that, at the levels studied, the parameter that affects the electrical resistivity of graded composites most significantly is infiltration process temperature followed by SiO_2 crystallinity. Their relative contribution to the variance in the electrical resistivity values are 22 and 16%, respectively. The reason of proposing temperature as a main governing parameter could be its important role in formation of new ceramic phases in composite. In-situ formation of phases like spinel, magnesium oxide and aluminum nitride can reduce the electrical conductivity of matrix due to consumption of aluminum alloys during their formation.

Considering the tested parameters and levels, the maximum electrical resistivity can be obtained by using the process parameters shown in Table 15. When using these process parameters, the projected electrical resistivity is 0.0017 ± 0.0008 Ω m.

The verification test has been done according to the optimum parameters proposed by ANOVA for maximum electrical resistivity. The measured electrical resistivity was 0.0019 ± 0.0003 Ω m. This result is in good agreement with the projected values (0.0017 ± 0.0008 Ω m).

3.4. Thermal diffusivity

Thermal diffusivity (α with the unit mm^2/s) is a material-specific property for characterizing unsteady heat conduction. This value describes how quickly a material reacts to a change in temperature. Thermal diffusivity controls the time rate of temperature change as heat passes through a material. It is a measure of the rate at which a body with a nonuniform temperature reaches a state of thermal equilibrium. Under real conditions or in specific applications, temperatures are not held constant, which means that thermal transfer through the material decreases the thermal gradient. Under such conditions, thermal diffusivity becomes important.

Fig. 13 (a) shows the thermal diffusivity of the main starting materials in this investigation [29–31]. For non-metallic solids, the

Table 14
Pooled ANOVA table for maximum electrical resistivity of Al/SiC/RHA composite.

Column	Factors	Sum of squares	Variance	Contribution percentage
1	Temperature	1.51E-06	71E-07	22
2	Time	4.35E-07	2E-07	6
3	Temperature × Time	8.23E-07	4.E-07	12
4	Particle Size	2.31E-07	5E-07	3
5	Porosity	8.37E-07	4E-07	12
6	Alloy	8.23E-07	4E-07	12
7	Porosity × Time	6.67E-08	Pooled	Pooled
8	SiO_2 Content	3.88E-07	2E-07	5
9	Phase of SiO_2	1.10E-06	5E-07	16
Error		84E-07		12
Total		6.74E-06		

Table 15
Optimum process parameters for maximum electrical resistivity of Al/SiC/RHA composite.

Parameters	Proposed levels
Temperature (°C)	1300
Time (min)	150
Particle size (μm)	10 μm/129 μm
Porosity (%)	50–50
Phase of SiO_2	Amorphous
Alloy	High Mg
SiO_2 content (wt%)	10

heat transfer is view as being transferred via lattice vibration, as atoms vibrating more energetically at one part of a solid transfer that energy to less energetic neighboring atoms. This can be enhanced by cooperative motion in the form of propagating lattice waves, which in the quantum limit are quantized as phonons. As it was expected both fabricated alloys have less thermal diffusivity values than pure aluminum. Alloying causes distortion of structure which makes the movement of electrons difficult through the atoms [26]. Thus, diffusion of electrons decreases with increasing the content of alloying elements.

Fig. 13 (a) shows the temperature-dependence of thermal diffusivity of SiC, the roughly T^{-1}-dependence diffusivity for SiC, suggesting a dominant phonon conduction behavior, which resembles most polycrystalline materials [32]. As it can be seen, the difference between values became smaller at elevated temperatures, e.g. ~12% at 800 °C. This difference in thermal diffusivity may be the result of a number of factors such as impurity, grain size, crystal boundary, etc. [33]. Charvat and Kingery [34], reported that the presence of impurity causes a considerable reduction in thermal conduction properties, even when contamination is below 1%. As a matter of fact, impurities usually have a significant effect on the thermal conduction of highly pure polycrystalline, as well as single-crystal, solids [35].

Thermal diffusivity values for all fabricated Al/SiC/RHA over the time are presented in Fig. 13(b). As it can be seen fabricated composites according to the configurations 3, 8 and 9 have the highest thermal diffusivity values, respectively. Considering the fabrication parameters of composites with highest thermal diffusivity postulate that a combination of low reactive materials and use of preform with higher amount of SiC can results in fabrication of composite with high thermal diffusivity. L3 composite benefits from low Mg alloys and Crystal type II silica which both has a less reactivity in comparison to High Mg alloy and amorphous or Crystal type 1, respectively. Therefore, the percentage of aluminum matrix in final composite will be remained high.

On the other hand, all these three-mentioned composites were fabricated in low temperature which causes to less reaction between the components. L8 composite although is fabricated from High Mg allot and amorphous silica, its unique SiC architecture (Combination of fine and large SiC particles with high thermal diffusivity) makes it a composite with high value of thermal diffusivity. Also, the content of silica is 10 wt% of reinforcement which means the final composite is reinforced mainly with SiC particles.

4. Conclusions

Based on the results and carried out discussion, within the framework of the experimental design, with the parameters and levels defined for this project, the following conclusions can be drawn:

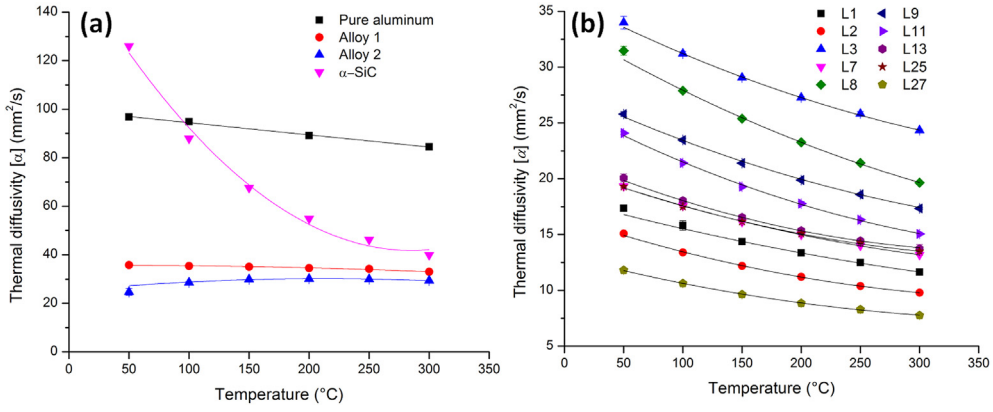

Fig. 13. Thermal diffusivity of (a) pure aluminum [29,30], α-SiC [31], alloy 1 (low Mg) and 2 (high Mg), and (b) Al/SiC/RHA bilayer fabricated composites at different temperatures.

1. The parameter that most significantly affects the modulus of elasticity of Al/SiC/RHA bilayer composites is processing time, with contribution percentages of 68 and 27% calculated from stress-strain graphs and ultrasonic method, respectively. However, the factor which mostly affects bending strength, CTE value and electrical resistivity of composites is process temperature with contribution percentages of 32, 28, and 22%, respectively. It is to visualize that temperature can affect all possible reactions which may occur during the process and that formation of each phase can substantially change the final properties of the composite. In the lower temperature range, formation of MgO is more possible while at higher temperatures, MgO can be replaced by $MgAl_2O_4$. Also, formation of AlN can be intensified by increasing the process temperature and time which can produce a composite with low CTE value and high electrical resistivity (L27).
2. The projected values for modulus of elasticity (170 GPa), porosity content (2.0%), bending strength (369 MPa), CTE (8.9×10^{-6}/°C) and electrical resistivity (0.0019 Ω m) of Al/SiC/RHA composites are in excellent agreement with those obtained in the verification tests under the optimal conditions according to ANOVA. The differences between the corresponding values obtained in verification tests and those of projected values, for bending strength, porosity content, modulus of elasticity (obtained from both methods) and CTE are below 5%, while that for electrical resistivity is 11%.
3. Al/SiC/RHA composites with electrical resistivity (2.02×10^{-3} Ω m) in the range of semiconductor materials (10^{-10} Ω m < σ < 10 Ω m) can be produced by processing porous preforms of 10 wt% amorphous silica (L27) with the Al-13Si-9Mg alloy at 1300 °C for 150 min.

Acknowledgment

Mr. Amin Bahrami and Ms. Niloofar Soltani gratefully acknowledge Conacyt (National Council of Science and Technology, in Mexico) for granting a doctoral scholarship. The authors are also thankful to Cinvestav IPN-Saltillo for support in the research activities in the field of advanced materials.

References

[1] A.L. Geiger, D.P.H. Hasselman, P. Welch, Electrical and thermal conductivity of discontinuously reinforced aluminum composites at sub-ambient temperatures, Acta Mater. 45 (1997) 3911–3914.
[2] N. Soltani, H.R. Jafari Nodooshan, A. Bahrami, M.I. Pech-Canul, W. Liu, G. Wu, Effect of hot extrusion on wear properties of Al–15 wt.% Mg_2Si in situ metal matrix composites, Mater. Des. 53 (2014) 774–781.
[3] N. Soltani, M.I. Pech-Canul, A. Bahrami, Effect of 10Ce-TZP/Al_2O_3 nanocomposite particle amount and sintering temperature on the microstructure and mechanical properties of Al/(10Ce-TZP/Al_2O_3) nanocomposites, Mater. Des. 50 (2013) 85–91.
[4] W.R. Mohn, D. Vukobratovich, Recent applications of metal matrix composites in precision instruments and optical systems, OPTICE 27 (1988), 270290–270290.
[5] C. Zweben, Advances in composite materials for thermal management in electronic packaging, JOM 50 (1998) 47–51.
[6] C. Zweben, Metal-matrix composites for electronic packaging, JOM 44 (1992) 15–23.
[7] J.M. Molina, J. Narciso, L. Weber, A. Mortensen, E. Louis, Thermal conductivity of Al–SiC composites with monomodal and bimodal particle size distribution, Mater. Sci. Eng. A 480 (2008) 483–488.
[8] S.Y. Oh, J.A. Cornie, K.C. Russell, Wetting of ceramic particulates with liquid aluminum alloys: Part II. Study of wettability, MTA 20 (1989) 533–541.
[9] M.I. Pech-Canul, R.N. Katz, M.M. Makhlouf, Optimum conditions for pressureless infiltration of SiCp preforms by aluminum alloys, J. Mater. Process. Technol. 108 (2000) 68–77.
[10] A. Bahrami, M.I. Pech-Canul, C.A. Gutierrez, N. Soltani, Effect of rice-husk ash on properties of laminated and functionally graded Al/SiC composites by one-step pressureless infiltration, J. Alloys Compd. 644 (2015) 256–266.
[11] A. Bahrami, U. Simon, N. Soltani, S. Zavareh, J. Schmidt, M.I. Pech-Canul, A. Gurlo, Eco-fabrication of hierarchical porous silica monoliths by ice- templating of rice husk ash, Green Chem. (2016), http://dx.doi.org/10.1039/C6GC02153K.
[12] N. Soltani, A. Bahrami, M.I. Pech-Canul, L.A. González, Review on the physicochemical treatments of rice husk for production of advanced materials, Chem. Eng. J. 264 (2015) 899–935.
[13] A. Bahrami, N. Soltani, M.I. Pech-Canul, C.A. Gutiérrez, Development of metal-matrix composites from industrial/agricultural waste materials and their derivatives, Crit. Rev. Environ. Sci. Technol. 46 (2016) 143–208.
[14] A. Bahrami, M.I. Pech-Canul, C.A. Gutiérrez, N. Soltani, Wetting and reaction characteristics of crystalline and amorphous SiO2 derived rice-husk ash and SiO_2/SiC substrates with Al–Si–Mg alloys, Appl. Surf. Sci. 357 (2015) 1104–1113. Part A.
[15] R. Roy, A Primer on the Taguchi Method, SME, 2010.
[16] A. International, ASTM C1161–13, Standard Test Method for Flexural Strength of Advanced Ceramics at Ambient Temperature, West Conshohocken, PA, 2013.
[17] Q. Hou, R. Mutharasan, M. Koczak, Feasibility of aluminium nitride formation in aluminum alloys, Mater. Sci. Eng. A 195 (1995) 121–129.
[18] M.I. Pech-Canul, R. Katz, M. Makhlouf, Optimum parameters for wetting silicon carbide by aluminum alloys, Metall. Mat. Trans. A 31 (2000) 565–573.
[19] J. Baldo, W. Dos Santos, Phase transitions and their effects on the thermal diffusivity behaviour of some SiO_2 polymorphs, Ceramica 48 (2002) 172–177.
[20] M.P. Bauleke, How to solve the problems of body cracking and glaze popping in stoneware bodies, Kans. State Geol. Surv. Bull. (1977) 23–27.
[21] L. Huang, J. Kieffer, Amorphous-amorphous transitions in silica glass. I. Reversible transitions and thermomechanical anomalies, Phys. Rev. B 69 (2004) 224203.
[22] M. Van Bommel, J. Van Lierop, Preparation of inorganic composite materials with an adjustable thermal expansion coefficient by the sol-gel method, J. Mater. Sci. Lett. 16 (1997) 448–450.
[23] M.-J. Zhu, L. Shun, Z. Xun, D.-G. Xiong, Laser-weldable Si–SiC/Al hybrid composites with bilayer structure for electronic packaging, Trans. Nonferrous Metals Soc. China 24 (2014) 1032–1038.
[24] S.Q. Wu, Z.S. Wei, S.C. Tjong, The mechanical and thermal expansion behavior of an Al–Si alloy composite reinforced with potassium titanate whisker, Compos. Sci. Technol. 60 (2000) 2873–2880.
[25] C.H. Hsueh, P.F. Becher, Thermal stresses due to thermal expansion anisotropy in materials with preferred orientation, J. Mater. Sci. Lett. 10 (1991) 1165–1167.
[26] W.W. Hintalla, The electrical conductivity of the copper-aluminum alloys, 1937.
[27] J.-i. Tani, H. Kido, Thermoelectric properties of Sb-doped Mg_2Si semiconductors, Intermetallics 15 (2007) 1202–1207.
[28] S. Angappan, L.J. Berchmans, C. Augustin, Sintering behaviour of $MgAl_2O_4$—a prospective anode material, Mater. Lett. 58 (2004) 2283–2289.
[29] J.E. Hatch, Aluminum: Properties and Physical Metallurgy, American Society for Metals, Ohi, 1984. Chap. 1.
[30] E.H. Buyco, F.E. Davis, Specific heat of aluminum from zero to its melting temperature and beyond. Equation for representation of the specific heat of solids, J. Chem. Eng. Data 15 (1970) 518–523.
[31] O. Nilsson, H. Mehling, R. Horn, J. Fricke, R. Hofmann, S.G. Müller, R. Eckstein, D. Hofmann, Determination of the thermal diffusivity and conductivity of monocrystalline silicon carbide (300-2300 K), High Temperatures, High. Press. 29 (1997) 73–79.
[32] W.D. Kingery, Thermal conductivity: XII, temperature dependence of conductivity for single-phase ceramics, J. Am. Ceram. Soc. 38 (1955) 251–255.
[33] D.-M. Liu, B.-W. Lin, Thermal conductivity in hot-pressed silicon carbide, Ceram. Int. 22 (1996) 407–414.
[34] F.R. Charvat, W.D. Kingery, Thermal conductivity: XIII, effect of microstructure on conductivity of single-phase ceramics, J. Am. Ceram. Soc. 40 (1957) 306–315.
[35] W.D. Kingery, M.C. McQuarrie, Thermal conductivity: I, concepts of measurement and factors affecting thermal conductivity of ceramic materials, J. Am. Ceram. Soc. 37 (1954) 67–72.